www.nature.com/aps

Acta Pharmacologica Sinica

ARTICLE

Lipid/PAA-coated mesoporous silica nanoparticles for dual-pH-responsive codelivery of arsenic trioxide/paclitaxel against breast cancer cells

Bing-bing Zhang[1], Xiao-jie Chen[1], Xu-dong Fan[1], Jing-jing Zhu[1], Ying-hui Wei[1], Hang-sheng Zheng[1], Hong-yue Zheng[2], Bin-hui Wang[3], Ji-gang Piao[1] and Fan-zhu Li[1]

Nanomedicine has attracted increasing attention and emerged as a safer and more effective modality in cancer treatment than conventional chemotherapy. In particular, the distinction of tumor microenvironment and normal tissues is often used in stimulus-responsive drug delivery systems for controlled release of therapeutic agents at target sites. In this study, we developed mesoporous silica nanoparticles (MSNs) coated with polyacrylic acid (PAA), and pH-sensitive lipid (PSL) for synergistic delivery and dual-pH-responsive sequential release of arsenic trioxide (ATO) and paclitaxel (PTX) (PL-PMSN-PTX/ATO). Tumor-targeting peptide F56 was used to modify MSNs, which conferred a target-specific delivery to cancer and endothelial cells under neoangiogenesis. PAA- and PSL-coated nanoparticles were characterized by TGA, TEM, FT-IR, and DLS. The drug-loaded nanoparticles displayed a dual-pH-responsive ($pH_e = 6.5$, $pH_{endo} = 5.0$) and sequential drug release profile. PTX within PSL was preferentially released at $pH = 6.5$, whereas ATO was mainly released at $pH = 5.0$. Drug-free carriers showed low cytotoxicity toward MCF-7 cells, but ATO and PTX co-delivered nanoparticles displayed a significant synergistic effect against MCF-7 cells, showing greater cell-cycle arrest in treated cells and more activation of apoptosis-related proteins than free drugs. Furthermore, the extracellular release of PTX caused an expansion of the interstitial space, allowing deeper penetration of the nanoparticles into the tumor mass through a tumor priming effect. As a result, FPL-PMSN-PTX/ATO exhibited improved in vivo circulation time, tumor-targeted delivery, and overall therapeutic efficacy.

Keywords: mesoporous silica nanoparticles; arsenic trioxide; paclitaxel; breast cancer; polyacrylic acid; pH-responsive

Acta Pharmacologica Sinica (2021) 42:832–842; https://doi.org/10.1038/s41401-021-00648-x

INTRODUCTION

Cancer is considered one of the leading causes of death worldwide [1]. However, as a major clinical treatment option, chemotherapy has various severe side effects due to excessive and nondiscriminatory toxicity in healthy tissues [2]. Paclitaxel (PTX) has been widely used as a first-line anticancer drug and clinically used as a potent antineoplastic agent with broad cytotoxicity against multiple solid tumors (e.g., breast, ovarian, lung, prostate, and other cancers) that exerts cytotoxic effects and induces apoptosis through microtubule function interference and mitosis alteration [3], but it is limited in clinical chemotherapy treatment due to its severe multidrug resistance [4]. Combination therapy with other chemotherapeutic agents with similar or antagonistic effects could be an appropriate way to overcome its limits [5, 6]. It has been reported that arsenic trioxide (ATO) can reduce the multidrug resistance of tumor cells via multiple mechanisms, suggesting its potential as part of a combination regimen with PTX [7, 8]. ATO has been approved by the Food and Drug Administration (FDA) for the treatment of acute promyelocytic leukemia [9]. ATO also induces apoptosis and may have broad utility in other cancers [10–12]. Braguer et al. [13] reported that the combined use of ATO and PTX could promote the apoptosis of cancer cells, showing that microtubules and mitochondria are involved in the antagonistic activities of ATO and PTX. However, due to the differences in the pharmacologic, pharmacokinetic, and pharmacodynamic properties of the sea-gents, the synergistic effect achieved in vitro may not translate to in vivo applications. Therefore, the treatment may be compro-mised [14, 15]. Multiple agents have achieved therapeutic effects against cancer cells through different action mechanisms that can efficiently induce suppression of drug resistance and increase therapeutic efficacy [16–19]. Consequently, codelivery of multiple therapeutic agents has displayed huge advantages for cancer therapy over individual treatment [20–23].

In recent decades, nanomedicine has attracted increasing attention and emerged as a safer and more effective modality in cancer treatment than conventional chemotherapy [24–28]. Nanoparticles have displayed superior physicochemical properties

[1]College of Pharmaceutical Sciences, Zhejiang Chinese Medical University, Hangzhou 310053, China; [2]Libraries of Zhejiang Chinese Medical University, Zhejiang Chinese Medical University, Hangzhou 310053, China and [3]The Affiliated Municipal Hospital of Taizhou University, Taizhou 318000, China
Correspondence: Bin-hui Wang (wbh105@sina.com) or Ji-gang Piao (jgpiao@zcmu.edu.cn) or Fan-zhu Li (lifanzhu@zcmu.edu.cn)
These authors contributed equally: Bing-bing Zhang, Xiao-jie Chen

Received: 14 November 2020 Accepted: 12 March 2021
Published online: 6 April 2021

due to their tunable size at the nanoscale, ability to envelop both hydrophilic and hydrophilic agents, ease of functionality, and passive targeting through the enhanced permeability and retention (EPR) effect [29]. In particular, the distinction of the tumor microenvironment (TME) and normal tissues is often used in stimulus-responsive drug delivery systems for the controlled release of therapeutic agents at target sites [30, 31]. For example, the extracellular pH of the TME ($pH_e = 6.5–6.8$) is lower than that of normal tissues ($pH = 7.4$) due to insufficient oxygenation and further pH reduction inside late endosomes and lysosomes, which are often triggers for acid-responsive drug release [32–37].

Silica, as an endogenous substance, is considered "generally safe" by the FDA [38, 39]. Silica nanoparticle-based drugs have been implemented in human phase I clinical trials in recent years. Furthermore, the C-dot form of MSNPs was approved for a stage 1 clinical trial in 2014 [40, 41]. Mesoporous silica nanoparticles (MSNs) have been widely used as efficient drug carriers, with a focus on cancer-targeted drug delivery and TME-responsive drug release due to their ease of preparation, high surface area, and pore volume [42–46]. However, the applications of MSNs as a drug carrier have been restricted owing to burst release and poor stability [47]. Thus, identifying a simple and effective surface modification is essential to be found to improve relevant properties and make full use of the superb drug-loading capacity of MSNs. In recent years, due to the outstanding properties of liposomes, lipid-coated MSNs have been reported to be an ideal model for designing targeted codelivery nanosystems of anticancer therapeutics, enabling synergistic functional properties and mechanisms [48–52].

This study developed pH-sensitive lipid (PSL) and polyacrylic acid (PAA)-coated MSNs (FPL-PMSNs) for the coformulation of ATO (a water-soluble drug) and PTX (a highly lipophilic agent) (FPL-PMSN-PTX/ATO) for targeted delivery and controlled release to breast cancer cells both in vitro and in vivo. As a proof of concept, FPL-PMSN-PTX/ATO responded to both extracellular and endosomal/lysosomal pH values in a programmed and sequential release of PTX and ATO and displayed enhanced in vitro cytotoxicity and improved in vivo pharmacokinetics. As a result, codelivery of ATO and PTX to a specific target to exert a synergistic therapeutic effect against a murine breast cancer orthotopic transplantation model was achieved.

MATERIALS AND METHODS

Materials

Cetyltrimethylammonium bromide (CTAB), tetraethyl orthosilicate (TEOS), 4′,6-diamidino-2-phenylindole (DAPI), Phalloidin-Fluor 555, fluorescein isothiocyanate (FITC), and 3-(4,5-dimethylthiazol-2-yl)-2,5-diphenyltetrazolium bromide (MTT) were purchased from Sigma-Aldrich (St. Louis, MO, USA). (3-Aminopropyl) triethoxysilane (APTES) was obtained from Aladdin (Shanghai, China). Chloro (dimethyl)octadecylsilane was provided by Tokyo Chemical Industry Co., Ltd. (Shanghai, China). DSPE-PEG and CHEMS were supplied by Avanti (Shanghai, China). A Chemicon in vitro angiogenesis assay kit was purchased from Millipore (Massachusetts, USA). ATO (As_2O_3, 90%) was purchased from Alfa Aesar (Shanghai, China). PTX was obtained from Yuanye Biological Technology (Shanghai, China). Arsenic standard solution (1 mg/mL) was obtained from Beijing Century Audiocodes Biological Technology Co., Ltd. (Beijing, China). Annexin V-FITC/PI dual staining kit was purchased from BD (Oxford, UK).

Cell culture

Human umbilical vein endothelial cells (HUVECs) were kindly provided by Professor Gao at Zhejiang University. The human breast carcinoma cell line MCF-7 was purchased from ATCC, and cells were cultured with RPMI-1640 supplemented with 10% fetal bovine serum and 100 units/mL penicillin and streptomycin. The cells were cultured in a humidified atmosphere at 37 °C in 5% CO_2.

Preparation of FPL-PMSN-PTX/ATO

For the preparation of MSNs, 225-mg CTAB, 22.5-mL ethanol, and 150-mL ultrapure water were mixed in a 250-mL round bottom flask and subjected to ultrasonication for 20 min. Then, the pH was adjusted to 11.5 with 25% ammonia, and 1.25-mL TEOS was dropwise added and stirred into the mixture at 75 °C for 2 h. Then, the mixture was incubated for 24 h at room temperature and washed via centrifugation twice with ultrapure water (20,440 × *g*, 15 min). MSNs were obtained after the solution was dried in an oven at 60 °C and calcined at 550 °C for 6 h. MSNs (100 mg) were resuspended in 50-mL ethanol, after which 250-μL APTES was slowly added, and the mixture was stirred at 45 °C for 8 h. The NH_2-MSNs obtained were centrifuged and washed with ethanol (27220 × *g*, 30 min) three times. NH_2-MSNs (100 mg) were mixed with 0.5-mL chloro(dimethyl)octadecylsilanein 50-mL $CHCl_3$ and stirred for 12 h. The obtained NH_2-CMSNs was centrifuged and washed with hexane (48380 × *g*, 30 min) three times and dried in a vacuum. To prepare NH_2-CMSN-ATO, 40 mg of NH_2-CMSNs was dispersed into an aqueous solution of ATO (1 mg/mL) in a 25-mL round bottom flask and stirred at room temperature for 24 h. The NH_2-CMSN-ATO obtained was centrifuged and washed with water (48380 × *g*, 30 min). NH_2-CMSN-ATO (50 mg) was dispersed in 50-mL DMF, and 50-mg PAA was added before the solution was stirred at 100 °C for 2 h. The resulting PMSN-ATO was centrifuged and washed with deionized water three times (48,380 × *g*, 30 min). DSPE-PEG (32.5 mg), 1-mg F56, 10-mg CHEMS, and PTX were dissolved in 15-mL $CHCl_3$ and evaporated at 45 °C in a rotary evaporator for 20 min to remove $CHCl_3$. PMSN-ATO (10 mg) in 10-mL ethanol was added to dissolve the film, and the ethanol was evaporated at 45 °C for 20 min. FPL-PMSN-PTX/ATO was finally obtained after hydration with 10 mL of preheated ultrapure water (45 °C), sonication for 4 min, centrifugation (12,100 × *g*, 10 min) and three washes. Different ATO/PTX formulations were constructed by adjusting the amount of ATO and PTX added.

The in vitro release of ATO and PTX from PL-PMSN-PTX/ATO was investigated by using the dialysis bag method. Briefly, PL-PMSN-PTX/ATO was sealed in a dialysis bag (M_W 3500) and fully submerged into the release medium (100 mL, pH 7.4, 6.5 or 5.0). The release experiment was conducted at 37 °C with constant shaking. Samples were collected from the media at predetermined time intervals and instantly replaced with an equal volume of fresh PBS. ATO concentrations were measured by the inductively coupled plasma mass spectrometry (ICP-MS; iCAP-QC, Thermo Electron Corporation, Waltham, MA, USA) method, and PTX concentrations were detected by high-performance liquid chromatography (HPLC; 1260 Infinity II, Agilent, USA).

In vitro cytotoxicity and median-effect analysis

The cytotoxicity of NH_2-MSNs, NH_2-CMSNs, PMSNs, L-PMSNs, PL-PMSNs, and FPL-PMSNs, and the antitumor effects of various ATO/PTX formulations on MCF-7 cells were evaluated. Briefly, 8×10^3 MCF-7 cells in RPMI-1640 were seeded in 96-well plates and cultured at 37 °C for 24 h. Then, the cells were incubated with culture medium containing drug-free carriers or ATO/PTX formulations at various concentrations. After 48 h, the medium was replaced with fresh culture medium containing MTT (0.5 mg/mL), and cells were incubated for another 4 h. Then, the MTT was removed, and 150-μL DMSO was added. Relative cell viabilities were determined by measuring the absorbance in each well at 570 nm using a microplate reader (Synergy TM2, BIO-TEK Instruments Inc. USA).

The synergistic cytotoxic effect of ATO and PTX in MCF-7 cells was evaluated with Calcusyn software (Biosoft, England) based on Chou and Talalay's principle. The combination index (CI) of ATO

and PTX was calculated according to the two-drug combination equation as follows: $CI = 1/DRI_A + 1/DRI_P = D_A/D_{Ax} + D_P/D_{Px}$, where DRI_A and DRI_P denote the dose-reduction index of ATO and PTX, respectively, D_A and D_P denote the dose of ATO and PTX, respectively, in the combination therapy that kills x% of cells, D_{Ax} denotes the dose of ATO that kills x% of cells alone, and D_{Px} denotes the dose of PTX that kills x% of cells alone. The interaction between ATO and PTX was categorized based on the CI, where $CI < 1$, $CI = 1$, and $CI > 1$ indicates synergistic, additive, and antagonistic interactions, respectively.

Cell cycle and apoptosis analysis

MCF-7 cells (2×10^4) were seeded into six-well plates and cultured overnight at 37 °C. The cells were harvested after incubation with different concentrations of various ATO/PTX formulations for 24 h, followed by fixation with 70% ethanol for 8 h at 4 °C. Then, 1-mg/mL RNase A and 50-μg/mL propidium iodide (PI) were added and incubated for 30 min at 37 °C in the dark. Subsequently, cells were acquired and analyzed by flow cytometry with a Guava Easy Cytometer (Guava Easycyte, Merck Millipore, Darmstadt, Germany). All experiments were performed in triplicate.

The apoptosis of MCF-7 cells was determined using flow cytometry with an Annexin V-FITC/PI dual staining kit. Briefly, 5×10^5 cells were seeded in six-well plates and allowed to grow until they reached 80% confluence. After treatment with different ATO/PTX MSN formulations for 24 h, the cells were harvested and washed with PBS for subsequent Annexin-FITC staining for 20 min and PI staining for 10 min in the dark. Then, the cells were analyzed within 1 h of staining and analyzed with Modift software.

Western blotting

Western blotting experiments were used to evaluate the expression of the apoptosis-related proteins Bcl-2, Caspase-7, Cleaved Caspase-7, Cyclin B-1, Cyclin D-1, Caspase-9, Cleaved Caspase-9, cdc2, and P-cdc2; β-actin served as a loading control. Briefly, MCF-7 cells were seeded in six-well plates at a density of 5×10^5 cells/well and cultured for 24 h at 37 °C. The different ATO/PTX MSN formulations in fresh medium were added to the cells and incubated for 24 h. The proteins were extracted, denatured at 98 °C, and analyzed according to the standard Western blotting protocol.

In vitro cellular uptake and intracellular distribution

The intracellular localization of coumarin-6-loaded nanoparticles in MCF-7 cells was detected by confocal laser scanning microscopy (CLSM, Olympus, Tokyo, Japan). Cells were cultured in chambered coverslips at a density of 4×10^5 cells/well for 24 h, and then the medium was replaced with culture medium containing coumarin-6-loaded nanoparticles at coumarin-6 concentrations of 0.2 or 0.4 μg/mL and incubated for 2 h. Cells were then washed with PBS three times, fixed with 4% paraformaldehyde, and counterstained with DAPI and Phalloidin-Fluor 555 before observation.

To quantitatively analyze the cellular uptake of nanoparticles, 2×10^5 MCF-7 cells were seeded in six-well plates. When the cells reached ~80% confluence, the medium was replaced by culture medium containing coumarin-6-loaded nanoparticles comprising PL-PMSN and FPL-PMSN or FPL-PMSN (which were preincubated with free F56 for 30 min). The coumarin-6 concentrations were 0.2 or 0.4 μg/mL. After incubation for 2 h, the nanoparticle-containing medium was removed, cells were washed three times with PBS, and the fluorescence intensity was determined by flow cytometry.

3D tumor spheroid penetration and endothelial cell tube formation assay

To establish a tumor spheroid model, MCF-7 cells were seeded at a density of 5×10^3 cells/well into a 96-well plate pretreated with 2% low-melting agarose, followed by centrifugation ($1000 \times g$, 10 min) to promote spheroid formation. The progress was monitored under a microscope, and the cells were ready for treatment after 7 days. Then, coumarin-6-loaded nanoparticles of FPL-PMSN, FPL-PMSN-PTX, and FPL-PMSN-ATO were incubated with spheroids for 24 h, after which the cells were washed with PBS three times and fixed with 4% paraformaldehyde in PBS. Finally, the treated spheroids were subjected to confocal microscopy at different depths (20, 40, 60, and 80 μm) to evaluate the penetration of coumarin-6-loaded nanoparticles.

The HUVEC tube formation assay was performed with a Chemicon in vitro angiogenesis assay kit. In brief, 50-μL chilled Matrigel was added to each well of a precooled 96-well plate and then incubated at 37 °C for 1 h to solidify. HUVECs were seeded on the Matrigel at a density of 1×10^5 cells/well and then cultured in medium supplemented with saline, PTX, PL-PMSN, and FPL-PMSN for 10 h.

In vivo pharmacokinetics and distribution studies

All animal procedures complied with the guidelines of the Zhejiang Chinese Medical University Animal Care and Use Committee. Fifteen tumor-bearing female ICR mice were randomly divided into three groups. To evaluate the pharmacokinetics of the nanoparticles, 200 μL of 1-mg/kg ATO, NH_2-CMSN-ATO, PMSN-ATO, L-PMSN-PTX/ATO, PL-PMSN-PTX/ATO, or FPL-PMSN-PTX/ATO was administered via tail vein injection. Blood samples were collected at different time intervals following injection and subjected to ICP-MS.

To study the biodistribution of the nanoparticles in various tissues, fifteen tumor-bearing ICR mice were randomly divided into three groups and injected with FITC-labeled L-PMSN-PTX/ATO, PL-PMSN-PTX/ATO, or FPL-PMSN-PTX/ATO. Twenty-four hours after injection, the mice were euthanized, and their liver, kidney, spleen, lung, heart, and tumor were collected from each mouse and subjected to imaging with an IVIS Spectrum Imaging System (Perkin Elmer, Waltham, Massachusetts, USA). The fluorescence intensity was quantified.

In vivo tumor vessel targeting and penetration study

For the tumor vessel targeting study, mice bearing MCF-7-derived tumors were intravenously injected with 200-μL L-PMSN-PTX/ATO, PL-PMSN-PTX/ATO, or FPL-PMSN-PTX/ATO labeled with coumarin-6 (coumarin-6 concentration: 1 mg/kg). The mice were sacrificed at 24 h after administration, and cryostat sections (8 μm) of the tumor were prepared. CD31-labeled antibody was used to stain the tumor vasculature as described by Wang et al. [1]. Then, the slides were observed under CLSM.

MCF-7 tumor-bearing mice were intravenously injected with 200-μL L-PMSN-PTX/ATO, PL-PMSN-PTX/ATO, or FPL-PMSN-PTX/ATO labeled with coumarin-6 (coumarin-6 concentration: 1 mg/kg). After 24 h, the mice were sacrificed, and cryostat sections (8 μm) of the tumor were prepared for further observation under an Olympus Macro Zoom Microscope (VS120-S6-W, OLYMPUS, Japan).

In vivo antitumor evaluation

On day 1, MCF-7 tumor-bearing mice with a tumor volume of ~100 mm^3 were randomly divided into seven groups ($n = 5$ per group), and each group was injected with saline, NH_2-CMSN-ATO, PMSN-ATO, a mixture of ATO and PTX, L-PMSN-PTX/ATO, PL-PMSN-PTX/ATO, and FPL-PMSN-PTX/ATO via tail vein every 2 days at a dose of ATO: 1 mg/kg and PTX: 0.5 mg/kg. During the subsequent 24-day treatment period, the tumor volumes and body weights of the mice were recorded every other day. After the treatment, the mice were sacrificed, and major organs, including the heart, liver, spleen, lung and kidney, and tumor, were collected. Organ tissue sections were subjected to hematoxylin

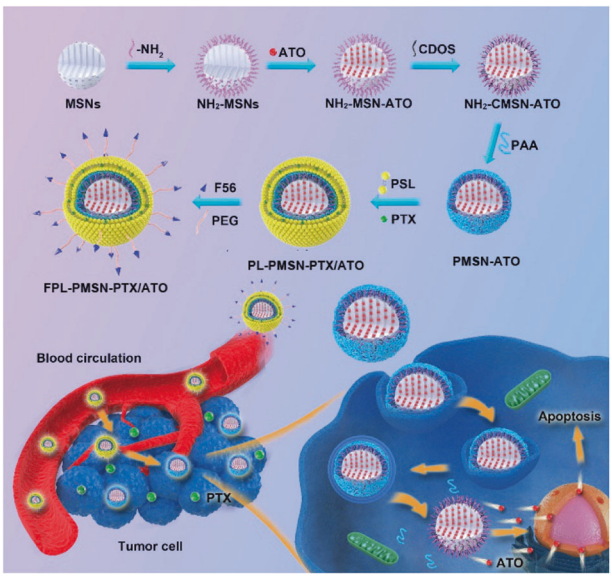

Fig. 1 Schematic illustration of the preparation process of FPL-PMSN-PTX/ATO, the blood circulation, the accumulation at the tumor site, and the preferential release of PTX at pH_e and ATO at pH_{endo}.

and eosin (H&E) staining, and tumor tissue sections from each group were subjected to TUNEL and Ki67 staining.

Statistical analysis

Data were presented as mean ± standard deviation. Statistical significance was determined by SPSS 20. $P < 0.05$ was considered to be statistically significant, and a extreme significance was indicated by $P < 0.01$.

RESULTS AND DISCUSSION

FPL-PMSN was designed to achieve targeted codelivery of ATO and PTX (Fig. 1). ATO was loaded into the nanochannels of MSNs, and PTX was inserted into the lipid bilayer membrane, which also sealed the pores of the MSNs and prevented a burst release of ATO. The presence of polyethylene glycol (PEG)-modified lipids prolonged the circulation time of the drug-loaded MSNs and reduced the immunogenicity of MSNs, thereby facilitating accumulation at the tumor site via the EPR effect. Furthermore, functionalization with a tumor-targeting peptide (F56) at the extremity of PEG enabled target-specific delivery to cancer cells and sites of neoangiogenesis [53]. Upon encountering to the tumor site, PSL responded to the extracellular pH (pH = 6.5–6.8) to preferentially release PTX, whereas PAA was mainly disassembled at endosome/lysosome pH (pH = 5) to release ATO.

Characterization of FPL-PMSN-PTX/ATO

MSNs with a diameter of 117.7 ± 1.51 nm were prepared using the Stöbber method. MSNs displayed uniform and spherical morphology under a transmission electron microscope (TEM; Fig. 2a). Moreover, the Fourier transform infrared spectroscopy (FT-IR) spectra confirmed the composition of MSNs via the adsorption peak at 1083.82 cm^{-1}, which corresponds to the Si–O–Si asymmetric stretching vibration. In addition, the symmetric stretching and bending vibrations of the Si–O–Si adsorption peak were 800.33 and 462.84 cm^{-1}, respectively (Fig. 2e). Amine groups were introduced to both the internal and external surfaces of MSNs, as evidenced by the appearance of an adsorption peak at 1508.09 cm^{-1}. NH_2-MSNs had a slight increase in diameter of 124.3 ± 1.53 nm (Fig. 2c), and the zeta potential switched from −30.3 ± 1.15 to 37.3 ± 1.16 mV (Fig. 2d). The positively charged amines could absorb ATO and attract the COO functional groups of PAA. The successful modification of NH_2-MSN with CDOS was confirmed by the appearance of a C–H stretching absorbance at 2800–3000 cm^{-1} from $-CH_3$ in the FT-IR spectra (Fig. 2e). Surface attachment with CDOS brought about Van der Waals forces and hydrophobic interactions and enabled the association of hydrocarbon chains between the external CMSN and phospholipids. The formation of a core-shell structure in aqueous solutions stabilized MSNs within the circulation [54]. After ATO loading, the zeta potential of NH_2-CMSN-ATO decreased to 19.7 ± 0.58 mV due to partial neutralization of the charges by the drug molecules. A subsequent PAA layer was formed through electronic interactions between the NH_2-CMSN amine groups and the PAA carboxyl groups, which further increased the diameter to 149.7 ± 6.56 nm and decreased the zeta potential to 11.7 ± 1.01 mV (Fig. 2c, d). The presence of peaks at 1652 cm^{-1} in the FT-IR spectra indicated the successful formation of a PAA layer. The coating lipid was composed of DSPC, DSPE-PEG_{2000}, cholesterol, and cholesteryl hemisuccinate, which self-assembled and fused to the PMSN-ATO surface during hydration using surface-anchored octadecylsilane chains as a support, leading to the formation of PL-PMSN-PTX/ATO with an increased diameter of 169.7 ± 2.08 nm. The F56 peptide was added to the lipid bilayer to achieve targeted drug delivery to MCF-7 cells. The presence of the F56 peptide reduced the zeta potential to −35 mV, and the negative surface charges may reduce nonspecific interactions between nanoparticles and proteins within the blood. TEM characterization of FPL-PMSN-PTX/ATO further demonstrated the successful assembly of lipid bilayers with an intact lipid bilayer 9-nm thick (Fig. 2b).

The MSNs displayed a type-IV pattern in N_2 adsorption–desorption characterization. In addition, the specific surface area and the cumulative pore volume of the MSNs were 1203.453 m^2/g and 1.088 cm^3/g, respectively (Fig. 2f, g). Meanwhile, the pore size distribution of the MSNs was within a narrow distribution of 3.0 nm. Amine modification significantly reduced the specific surface area and the cumulative pore volume to 485.338 m^2/g and 0.474 cm^3/g, respectively. Subsequently, the specific surface area, cumulative pore volume, and pore size of MSNs were further reduced to 272.418 m^2/g, 0.216 cm^3/g, and 0.92 nm, respectively, after CDOS modification and PAA grafting. Finally, the lipid coating rendered all of these parameters undetectable, indicating a full blockage of the pores by the lipid bilayer. Thermogravimetric analysis was conducted to estimate the weight percentage of each component within the FPL-PMSNs (Fig. 2h). The percentage of weight loss of the MSNs, NH_2-MSNs, NH_2-CMSNs, PAA-NH_2-CMSNs, and PL-PMSNs was 96.36%, 86.07%, 82.06%, 78.03%, and 63.96%, respectively, when heated from 100 to 800 °C. Accordingly, the calculated weight percentages of the amine group, octadecylsilane, PAA, and lipid were 10.29%, 4.01%, 4.03%, and 14.07%, respectively.

In vitro cytotoxicity and median-effect analysis

Various formulations of PTX and ATO were tested against MCF-7 cells to identify and achieve the optimal drug ratio for maximal synergistic cytotoxicity and combined drug mechanisms. The outcomes were analyzed using the CI as the evaluation criteria for the median-effect analysis. The formulations of ATO:PTX at ratios of 1:1, 1:2, and 2:1 displayed better cell inhibition rates and smaller CIs than did the 1:4 formulation, indicating that further experiments should be performed to determine the best drug ratio that will achieve a synergistic effect (Fig. 3a–c).

Cell cycle and apoptosis analysis

MCF-7 cells were treated with various PTX-ATO formulations, stained with PI to analyze the cell-cycle distribution with flow cytometry and characterize the combined effect of PTX-ATO on cell

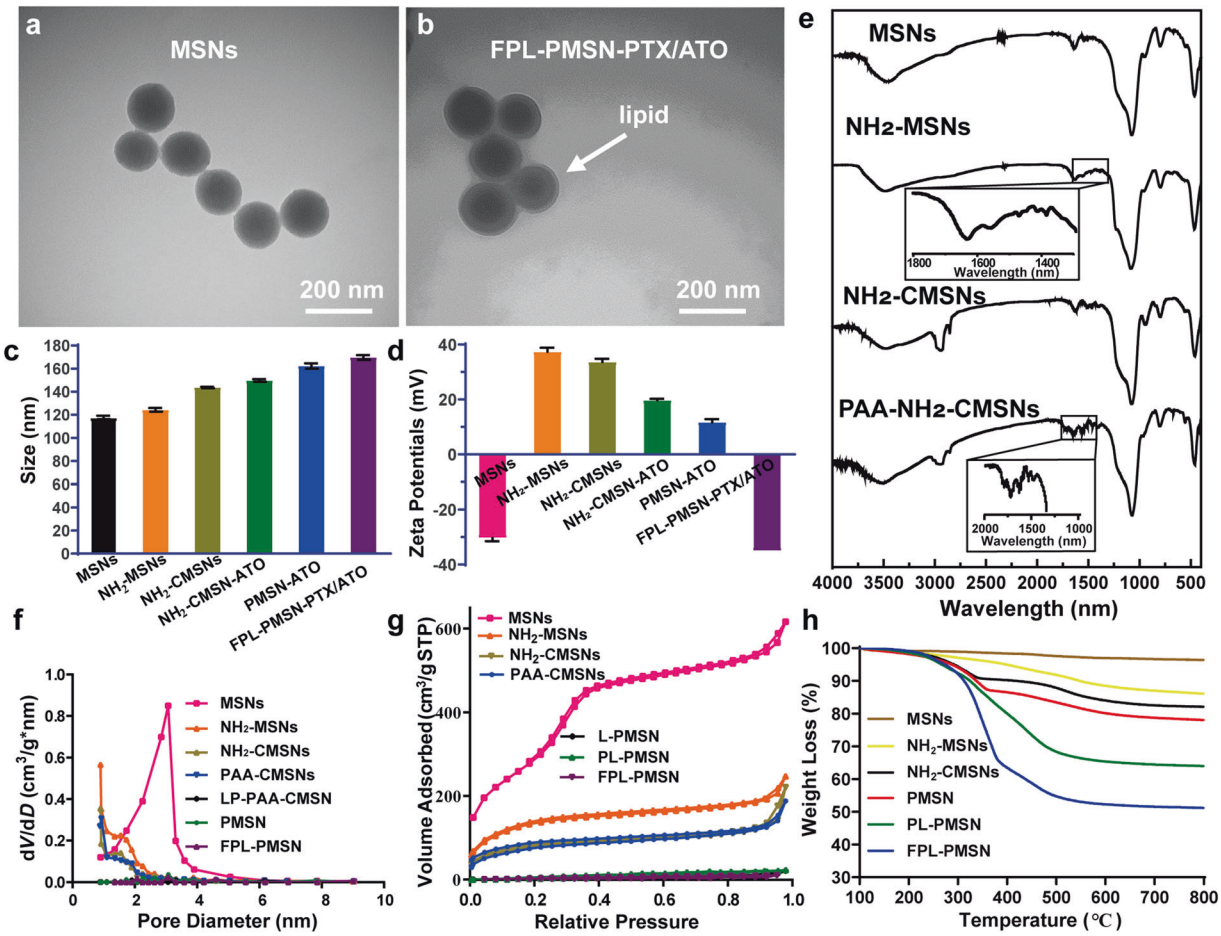

Fig. 2 Characterization of FPL-PMSN-PTX/ATO. TEM images of **a** MSNs and **b** FPL-PMSN-PTX/ATO. **c** Hydrodynamic diameters and **d** zeta potential of each obtained intermediate during preparation and the final product of FPL-PMSN-PTX/ATO. **e** FT-IR spectra of MSNs, NH_2-MSNs, NH_2-CMSNs, and PAA-NH_2-CMSNs. **f** Pore size distribution, **g** N_2 adsorption–desorption isotherm, and **h** thermogravimetric analysis of each obtained product during the preparation of FPL-PMSN-PTX/ATO.

inhibition (Fig. 3d). As a result, the formulations of ATO:PTX at ratios of 1:2 and 2:1 specifically arrested 29.5% and 29.9% of MCF-7 cells at G_2/M phase, respectively, which were higher than the percentages of cells arrested after single treatment with ATO (15.7%) or PTX (18.1%). These results showed that the combination of ATO and PTX synergistically inhibited the proliferation of MCF-7 cells via cell-cycle arrest and induced synergistic cytotoxicity.

Annexin V-FITC/PI staining-based flow cytometry analysis was performed to examine the apoptosis rate of the MCF-7 cells treated with ATO and PTX alone or in combination (Fig. 3e). After a 24-h treatment with different ATO/PTX formulations at various concentrations, treatments with ATO:PTX ratios of 1:2 and 2:1 resulted in 21.45% and 61.48% of apoptotic cells, both of which were significantly higher than the percentage of apoptotic cells after treatment with ATO or PTX alone (7.56% and 7.41%, respectively). Considering all these results, the ATO:PTX formulation at a ratio of 2:1 was selected for subsequent cellular and animal experiments.

Western blotting

To further confirm and evaluate the possible mechanism of synergistic action, the expression levels of apoptosis-related proteins in MCF-7 cells were determined using Western blotting analysis (Fig. 3f). The combination treatment of ATO and PTX displayed a superior inhibitory effect on the expression of Bcl-2, caspase-7, caspase-9, cyclin B-1, and cyclin D-1 compared with that in response to single treatment with either ATO or PTX. Furthermore, the involvement of caspase-7 and caspase-9 was clearly shown from the combination treatment, whereas that after either ATO or PTX treatment was negligible. In addition, the combination treatment also resulted in better activation and reduced phosphorylation of the cdc2 protein.

Drug loading and release behavior evaluation

PTX and ATO were loaded into the lipid bilayer and the nanochannels of the MSN nanoparticles, respectively. The respective loading efficiencies of PTX and ATO were 2.4% and 16.2% according to the HPLC and ICP-MS results, which was in correlation with our expectations. Cholesteryl hemisuccinate is an essential component of PSL, which becomes unstable at the extracellular pH of the TME, causing lipid disruption and PTX release. Furthermore, as a pH-responsive material, PAA protonates at pH < 5.5 and induces pH-responsive drug release. Thus, the PTX and ATO release profiles from PL-PMSN-PTX/ATO were then monitored in different pH environments (pH = 7.4, 6.5, or 5.5; Fig. 4a, b) using non-pH-responsive lipid-coated MSNs (L-PMSN-PTX/ATO) as a control (Figs. S1 and S2). Nearly 80% of ATO was released from NH_2-CMSN-ATO at all pH values (Fig. S1). PAA layer formation and the lipid coating significantly suppressed ATO release, and the release in response to pH was observed. At a physiological pH of 7.4, the release of PTX and ATO was 55.6% and 38.8%, respectively, and a sustained release profile was observed during the 48-h release

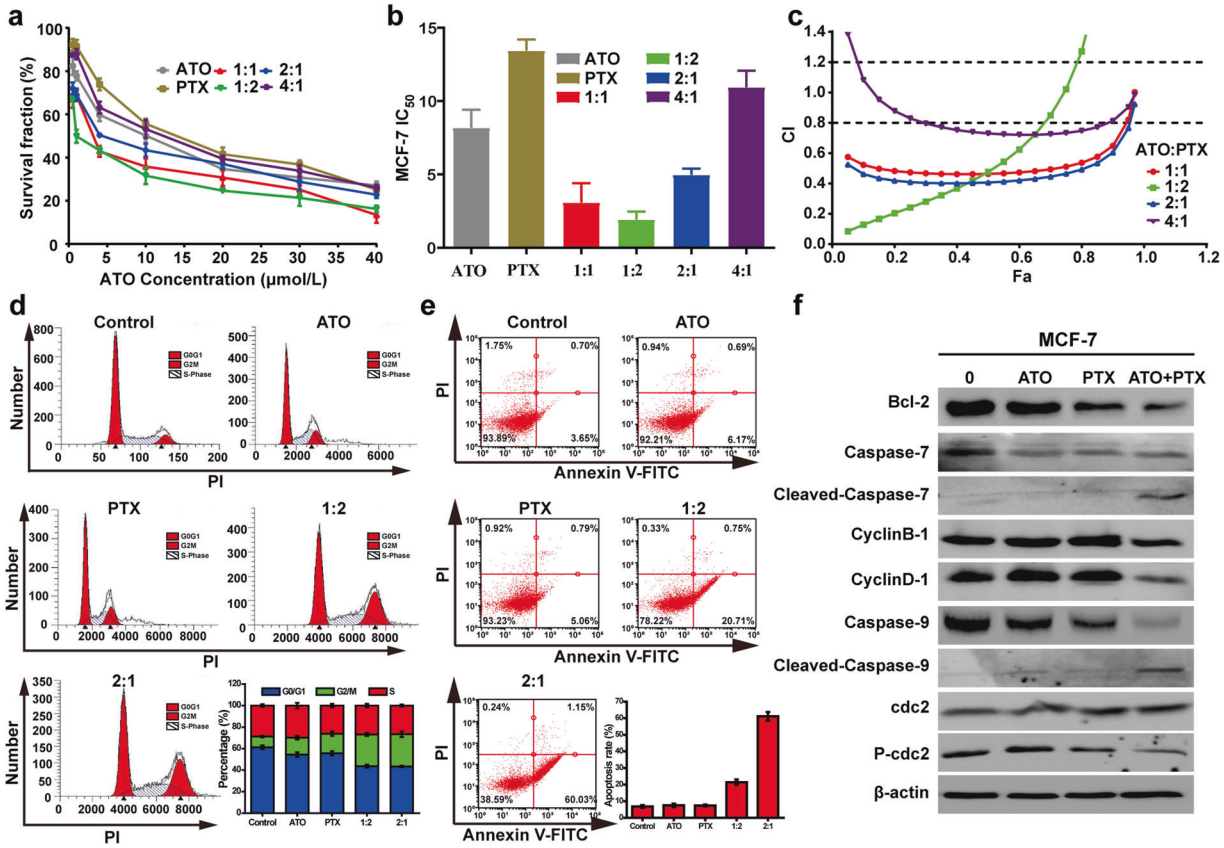

Fig. 3 In vitro synergistic therapeutic study. a Cell inhibition rate and **b** IC_{50} values of ATO and PTX when combined as various formulations. **c** Combination index values of ATO and PTX in various formulations. **d** Cell cycle and **e** apoptosis analysis of MCF-7 cells treated with various formulations of ATO and PTX. **f** Western blotting analysis of apoptosis-related proteins in MCF-7 cells treated with ATO and PTX either alone or in combination.

period. Faster PTX (77.1%) and ATO (63.1%) releases were observed at pH 6.5, which could be explained by lipid disruption. Thus, PTX was preferentially released at pH 6.5, and PAA grafting suppressed the release of ATO at pH > 5.0. At pH < 5.0, 76% and 97% of ATO and PTX were released, respectively, which is likely ascribed to the simultaneous effects of lipid disruption, the dissociation between the PAA and amine groups, and the contraction of the hydrated polymer upon partial protonation of the COO^- groups. In contrast, L-PMSN-PTX/ATO exhibited a similar release rate of ~60% at all tested pH values (Fig. S2). Thus, it can be concluded that PL-PMSN-PTX/ATO possesses pH-responsive drug release characteristics and enables a dual-pH-triggered sequential release profile of both enveloped drugs.

In vitro cytotoxicity evaluation

Cytotoxicity studies of PL-PMSN-PTX/ATO against MCF-7 cells were conducted at different concentrations with L-PMSN-PTX/ATO as a control. First, each component of PL-PMSN-PTX/ATO, including NH_2-MSNs, NH_2-CMSNs, PMSNs, LPs, PSLs, and FPLs, was incubated with MCF-7 cells. No sign of cytotoxicity was observed up to the 50-μg/mL concentration, which suggested that these components are intrinsically biocompatible (Fig. S3). Second, both PL-PMSN-PTX/ATO and FPL-PMSN-PTX/ATO were exposed to MCF-7 cells at various concentrations to evaluate their cytotoxicity. FPL-PMSN-PTX/ATO displayed a better antitumor efficiency than did PL-PMSN-PTX/ATO, which could be attributed to enhanced cellular uptake facilitated by the targeting ability of the F56 modification (Fig. 4c).

In vitro cellular uptake and intracellular distribution

The intracellular localization of coumarin-6-loaded PL-PMSN-PTX/ATO and FPL-PMSN-PTX/ATO in MCF-7 cells was detected by CLSM (Fig. 4d). FPL-PMSN-PTX/ATO displayed a significantly stronger fluorescence intensity than did the nanoparticles without the F56 modification, indicating that the presence of F56-targeting ligands enhanced the cellular uptake of the nanoparticles. In addition, the cellular uptake of FPL-PMSN-PTX/ATO significantly decreased if the cells were preincubated with free F56, indicating the targeting ability mediated by F56. The same results were observed in the flow cytometry profiles.

3D tumor spheroid penetration and endothelial cell tube formation assay

The tumor penetration of nanoparticles with or without PTX loading was evaluated in a 3D spheroid tumor model (Fig. 5a). Treatment of cells with apoptosis-inducing drugs could transiently enlarge the interstitial space and thereby promote the intratumoral diffusion of drugs delivered by the nanoparticles [55, 56]. Coumarin-6-coloaded FPL-PMSN with ATO or PTX was incubated with 3D spheroids and scanned via CLSM at different depths. Minimal fluorescence could be observed at a depth of 60 μm, illustrating that ATO loading did not improve the penetration of FPL-PMSN. However, coumarin-6 coloaded FPL-PMSN-PTX/ATO exhibited a strong green fluorescence signal as deep as 80 μm. It is believed that PSL could respond to the tumor extracellular pH_e and release loaded PTX, which would cause an enlargement of the

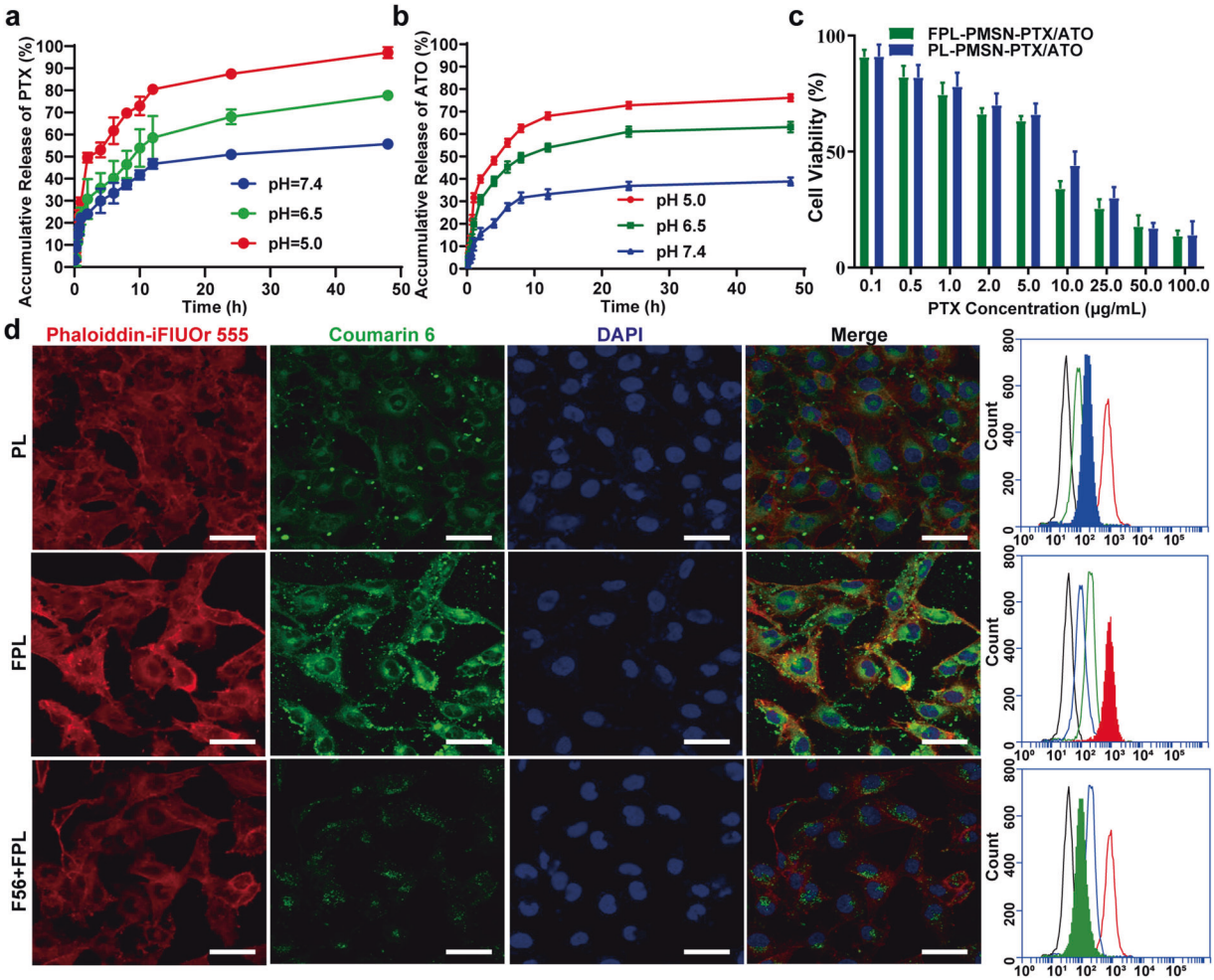

Fig. 4 In vitro release, cytotoxicity and cellular uptake study. The release profile of PTX (**a**) and ATO (**b**) from PL-PMSN-PTX/ATO at pH 7.4, 6.5, or 5.0. **c** Cytotoxicity of PL-PMSN-PTX/ATO and FPL-PMSN-PTX/ATO. **d** Confocal images and flow cytometry profiles of MCF-7 cells incubated with coumarin-6-loaded nanoparticles of PL-PMSN-PTX/ATO, FPL-PMSN-PTX/ATO, and F56 + FPL-PMSN-PTX/ATO. Scale bar = 20 μm.

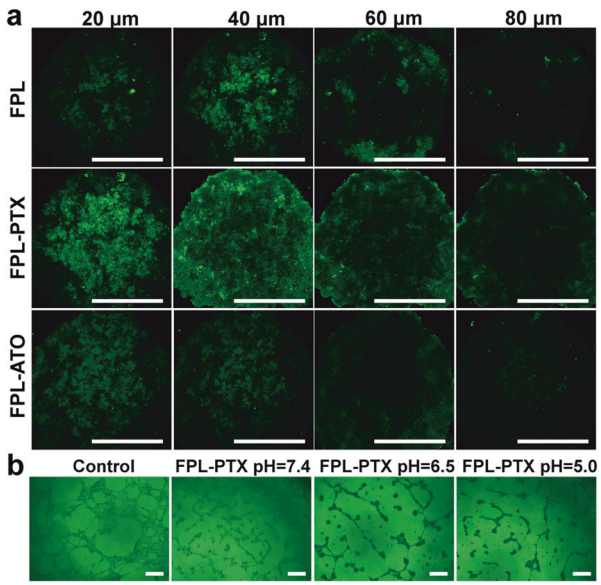

Fig. 5 In vitro penetration and anti-angiogenesis study. a 3D spheroids treated with FPL-PMSN, FPL-PMSN-PTX, and FPL-PMSN-ATO. Scale bar = 500 μm. **b** Endothelial cell tube formation assay with HUVECs incubated with FPL-PTX at pH 7.4, 6.5, or 5.0. Scale bar = 200 μm.

interstitial space, thus facilitating the deep penetration of nanoparticles into tumors and enhancing the bioavailability of PTX and ATO [57].

Consequently, an endothelial tube formation assay was conducted at various pH values to evaluate the inhibitory effect of PTX on the angiogenesis. Briefly, HUVECs were treated with PTX and FPL-PTX at pH 7.4, 6.5, or 5.0, and saline treatment was used as a control. FPL-PTX displayed a more potent inhibitory effect at pH 6.5 and 5.0, possibly due to the pH-responsive PTX release, than did free drug or FPL-PTX at pH 7.4 (Fig. 5b).

In vivo pharmacokinetics and distribution studies

To assess the in vivo pharmacokinetics of ATO, ATO-loaded nanoparticles (e.g., NH_2-CMSN-ATO, PMSN-ATO, L-PMSN-PTX/ATO, PL-PMSN-PTX/ATO, and FPL-PMSN-PTX/ATO) were intravenously injected into ICR mice, and blood was collected at different time intervals. The pharmacokinetics results over a 48-h period after intravenous injection are shown in Fig. 6a. ATO in saline was quickly cleared with a plasma concentration of 0.015 μg/mL at 48 h post administration, whereas amine modification and PAA grafting improved retention in blood (serum concentration 0.027 and 0.042 μg/mL, respectively). In addition, the lipid coating of LP or PSL resulted in further enhancement of blood retention. The plasma concentrations were 0.079 and 0.089 μg/mL, which were almost six- and two fold more than that of ATO in saline and PMSN-ATO, respectively, indicating

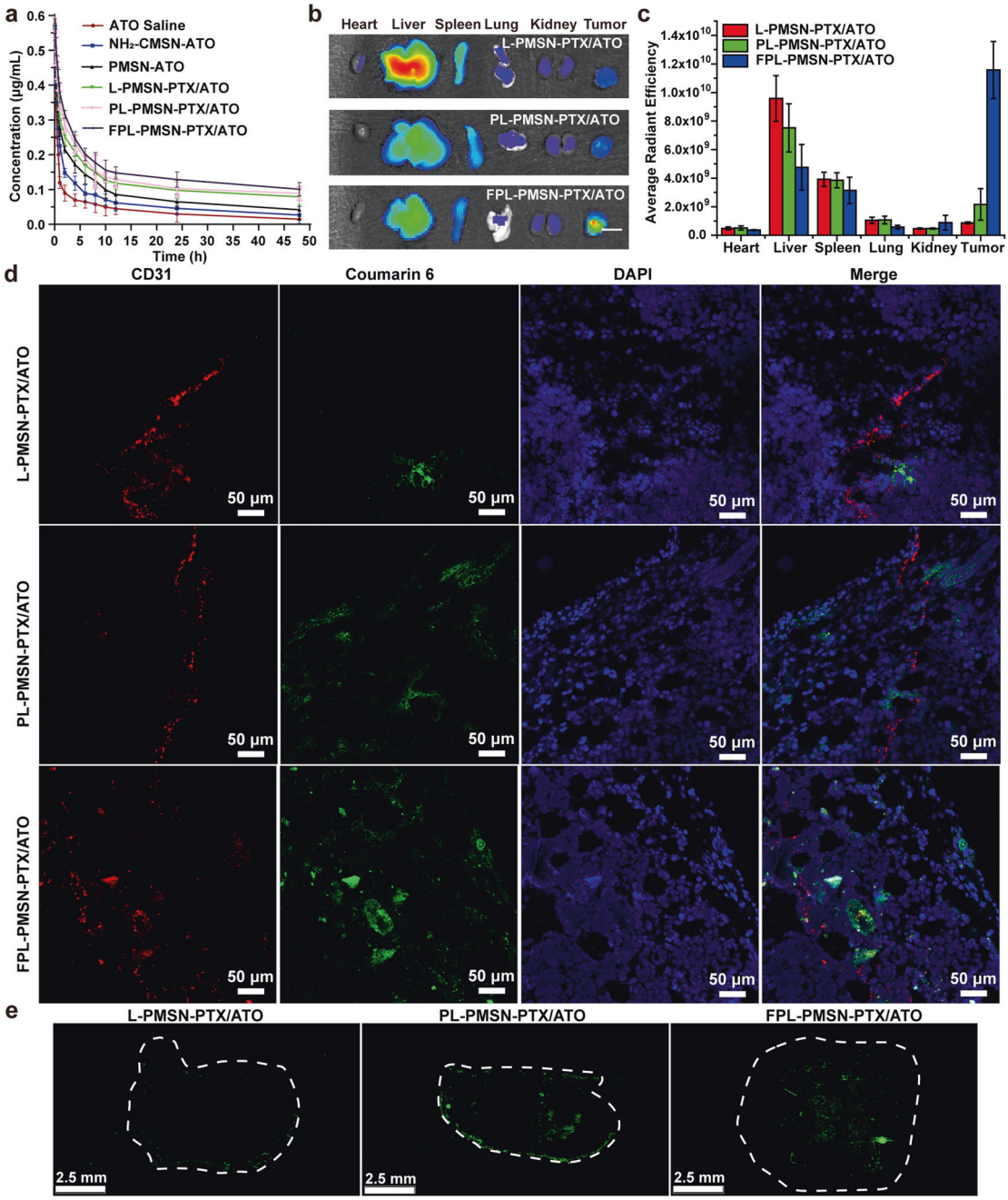

Fig. 6 In vivo biodistribution and penetration study. a Mean plasma drug concentration-time in rats. **b** Fluorescence images and **c** biodistribution of different formulations in major organs, including the heart, liver, spleen, lung and kidney, and tumors of mice 24 h after intravenous injection of L-PMSN-PTX/ATO, PL-PMSN-PTX/ATO, and FPL-PMSN-PTX/ATO. Scale bar = 0.5 cm. **d** Fluorescence distribution and **e** in vivo penetration at the tumor site at 24 h after administration of L-PMSN-PTX/ATO, PL-PMSN-PTX/ATO, and FPL-PMSN-PTX/ATO.

that lipid and PEG modifications prolonged the blood circulation of the nanoparticles. Extension of pharmacokinetic behavior by surface modification could allow for sustained systemic delivery, enhanced tumor uptake, and improved treatment efficiency.

A biodistribution study of FITC-labeled nanoparticles was conducted to monitor the in vivo behaviors. As depicted in Fig. 6b, c, the fluorescence signals of L-PMSN-PTX/ATO at 24 h after injection were primarily distributed in the liver and spleen, whereas a small signal was observed at the tumor site. Furthermore, PL-PMSN-PTX/ATO displayed slightly more accumulation in the tumor, a limited decrease in the liver, and unnoticeable changes in the spleen. However, FPL-PMSN-PTX/ATO displayed significantly enhanced accumulation approximately sixfold that of PL-PMSN-PTX/ATO, whereas much fewer nanoparticles were distributed within the liver and spleen, indicating improved biodistribution by the F56 modification.

In vivo tumor vessel targeting and penetration study

At 24 h after administration, the tumor sections were stained with CD31 and DAPI to evaluate in vivo tumor vessel targeting of the various formulations. As shown in Fig. 6d, compared with L-PMSN-PTX/ATO and PL-PMSN-PTX/ATO, FPL-PMSN-PTX/ATO exhibited higher fluorescence intensity around vessels

and broader distribution within the tumor site, benefiting from the binding affinity of F56 to sites of neoangiogenesis. Then, the penetration of various formulations in vivo was observed under an Olympus Macro Zoom Microscope (Fig. 6e). Little fluorescence was observed at the tumor site in the coumarin-6 coloaded L-PMSN-PTX/ATO group, while the PL-PMSN-PTX/ATO group exhibited a stronger green fluorescence signal due to the extracellular pH-sensitive release of PTX, leading to expansion of the interstitial space and deeper penetration of the nanoparticles. Furthermore, the strongest fluorescence of coumarin-6 could be seen inside tumors after treatment with FPL-PMSN-PTX/ATO, which should be achieved to enhance accumulation facilitated by the F56 modification and therefore strengthen the tumor priming effect achieved by PTX.

In vivo antitumor evaluation

Furthermore, in vivo therapeutic studies were performed on tumor-bearing mice (Fig. 7a–d). The results showed that the tumor volumes of the ATO-loaded NH_2-CMSN-ATO and PMSN-ATO treatments had comparable reductions in tumor growth and weight, respectively. Combination treatment of ATO and PTX without carriers exhibited a better antitumor effect than did treatment with either drug alone, which should be attributed to a synergistic interaction of ATO and PTX. However, the incidence of adverse effects, as indicated by body weight loss, was overwhelming, despite the cytotoxicity of these compounds against cancer cells (Fig. 7b). All other formulations kept the body weight relatively stable during the treatment, suggesting acceptable side effects. Moreover, treatment with PL-PMSN-PTX/ATO resulted in a smaller tumor volume than did L-PMSN-PTX/ATO, although ATO and PTX codelivery with MSNs with LP and PSL coatings significantly increased the antitumor efficacy. The F56 modification conferred the nanoparticles with targeting ability and selectivity and showed the best inhibitory effect on tumor growth (Fig. 7c, d). For the histopathology analysis, the results of the TUNEL and Ki67 staining indicated that FPL-PMSN-PTX/ATO caused more damage to the tumor than did either L-PMSN-PTX/ATO or PL-PMSN-PTX/ATO (Fig. 7e). Moreover, tumor damage caused by free ATO and PTX was better than that after single treatment with PMSN-ATO or NH_2-CMSN-ATO, suggesting the advantages achieved by codelivery of ATO and PTX. Histological analysis of the major organs (including the heart, liver, spleen, lung, and kidney) by H&E staining showed that the formulations of the delivery system did not cause noticeable damage compared with that observed after control treatment (Fig. 8).

CONCLUSION

In conclusion, a drug delivery system comprising FPL-PMSN-PTX/ATO based on MSNs with a double coating of PAA and PSL for synergistic delivery and dual-pH-responsive sequential release of ATO and PTX was formed. The codelivery of ATO and PTX loaded in nanoparticles demonstrated significant synergy for the effective treatment of MCF-7 cells through greater cell-cycle arrest and more activation of apoptosis-related proteins than single-drug treatment. In addition, improved in vivo circulation time, tumor-targeted delivery, and overall therapeutic efficacy were observed with in vivo experiments.

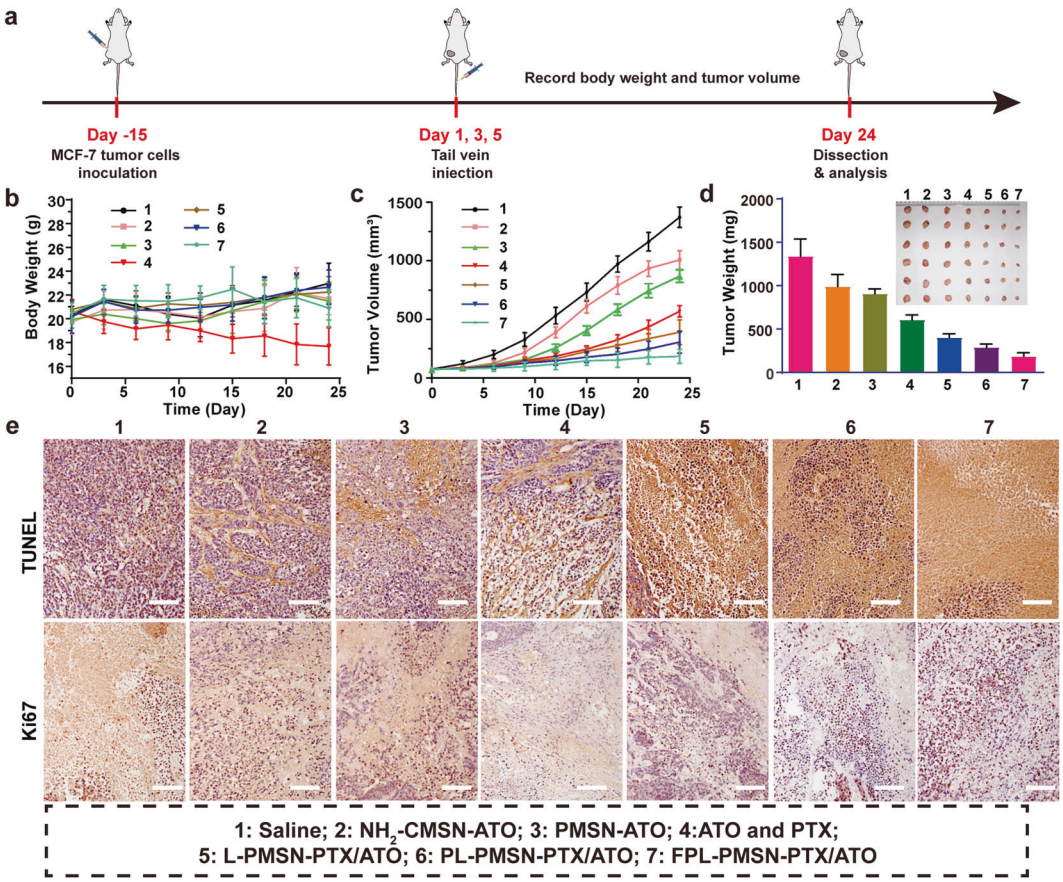

Fig. 7 In vivo antitumor study. a Schedule of cancer treatment. **b** Body weight curves, **c** tumor volume curves, and **d** tumor weight curves of the mice in different groups at the end of the treatment. **e** TUNEL and Ki67 staining of tumors after treatment with various formulations. Scale bar = 100 μm.

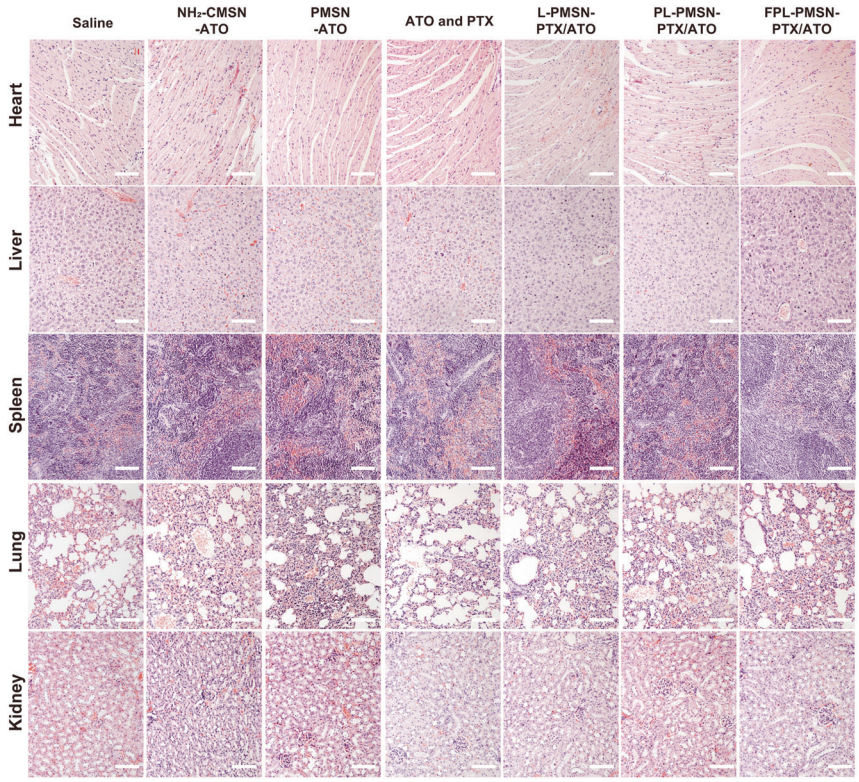

Fig. 8 H&E staining of major organs after treatment with various formulations. Scale bar = 100 μm.

ACKNOWLEDGEMENTS

This research was funded by the National Natural Science Foundation of China (No. 81873014 and 81873018), Natural Science Foundation of Zhejiang Province (LQ18E030003), Zhejiang Chinese Medical University School-level Scientific Research Fund Project (No. 2020ZG21).

AUTHOR CONTRIBUTIONS

FZL and BHW designed research; BBZ and XDF performed research; YHW, HSZ, and HYZ provided technical support and some instruments; XJC and JJZ analyzed data; JGP wrote the paper. All authors have read and approved the final manuscript.

ADDITIONAL INFORMATION

Supplementary information The online version contains supplementary material available at https://doi.org/10.1038/s41401-021-00648-x.

Competing interests: The authors declare no competing interests.

REFERENCES

1. Siegel RL, Miller KD, Jemal A. Cancer statistics, 2019. CA-Cancer J Clin. 2019;69:7–34.
2. Dong XY, Lang TQ, Yin Q, Zhang PC, Li YP. Co-delivery of docetaxel and silibinin using pH-sensitive micelles improves therapy of metastatic breast cancer. Acta Pharmacol Sin. 2017;38:1655–62.
3. Wang LG, Liu XM, Kreis W, Budman DR. The effect of antimicrotubule agents on signal transduction pathways of apoptosis: a review. Cancer Chemother Pharmacol. 1999;44:355–61.
4. Chen FY, Zhang Y, Chen XY, Li JQ, Xiao XP, Yu LL, et al. Development of a hybrid paclitaxel-loaded arsenite nanoparticle (HPAN) delivery system for synergistic combined therapy of paclitaxel-resistant cancer. J Nanopart Res. 2017;19. https://doi.org/10.1007/s11051-017-3848-0.
5. Filipits M. Mechanisms of cancer: multidrug resistance. Drug Discov Today Dis Mech. 2004;1:229–34.
6. Ghanbari P, Mohseni M, Tabasinezhad M, Yousefi B, Saei AA, Sharifi S, et al. Inhibition of survivin restores the sensitivity of breast cancer cells to docetaxel and vinblastine. Appl Biochem Biotech. 2014;174:667–81.
7. Zhao DF, Jiang YF, Dong XY, Liu ZL, Qu BB, Zhang YF, et al. Arsenic trioxide reduces drug resistance to adriamycin in leukemic K562/A02 cells via multiple mechanisms. Biomed Pharmacother. 2011;65:354–8.
8. Liu L, Li Y, Xiong XL, Qi K, Zhang C, Fang JP, et al. Low dose of arsenic trioxide inhibits multidrug resistant-related P-glycoprotein expression in human neuroblastoma cell line. Int J Oncol. 2016;49:2319–30.
9. Wang ZY, Chen Z. Acute promyelocytic leukemia: from highly fatal to highly curable. Blood. 2008;111:2505–15.
10. Miller WH, Schipper HM, Lee JS, Singer J, Waxman S. Mechanisms of action of arsenic trioxide. Cancer Res. 2002;62:3893–903.
11. Lu J, Chew EH, Holmgren A. Targeting thioredoxin reductase is a basis for cancer therapy by arsenic trioxide. Proc Natl Acad Sci U S A. 2007;104:12288–93.
12. Dilda PJ, Hogg PJ. Arsenical-based cancer drugs. Cancer Treat Rev. 2007;33:542–64.
13. Carre M, Carles G, Andre N, Douillard S, Ciccolini J, Briand C, et al. Involvement of microtubules and mitochondria in the antagonism of arsenic trioxide on paclitaxel-induced apoptosis. Biochem Pharmacol. 2002;63:1831–42.
14. Batist G, Gelmon KA, Chi KN, Miller WH, Chia SKL, Mayer LD, et al. Safety, pharmacokinetics, and efficacy of CPX-1 liposome injection in patients with advanced solid tumors. Clin Cancer Res. 2009;15:692–700.
15. Di MM, Chiodini P, Georgoulias V, Hatzidaki D, Takeda K, Wachters FM, et al. Meta-analysis of single-agent chemotherapy compared with combination chemotherapy as second-line treatment of advanced non-small-cell lung cancer. J Clin Oncol. 2009;27:1836–43.
16. Pushpalatha R, Selvamuthukumar S, Kilimozhi D. Nanocarrier mediated combination drug delivery for chemotherapy—a review. J Drug Deliv Sci Tec. 2017;39:362–71.
17. Wang MF, Wang JY, Li BC, Meng LX, Tian ZX. Recent advances in mechanism-based chemotherapy drug-siRNA pairs in co-delivery systems for cancer: a review. Colloid Surf B. 2017;157:297–308.
18. Dai X, Tan C. Combination of microRNA therapeutics with small-molecule anticancer drugs: mechanism of action and co-delivery nanocarriers. Adv Drug Deliv Rev. 2015;81:184–97.
19. Zhang CM, Zhang SB, Zhi DF, Cui JN. Cancer treatment with liposomes based drugs and genes co-delivery systems. Curr Med Chem. 2018;25:3319–32.
20. Eftekhari RB, Maghsoudnia N, Samimi S, Zamzami A, Dorkoosh FA. Co-delivery nanosystems for cancer treatment: a review. J Clin Oncol. 2019;7:90–112.
21. Zhang LF, Radovic-Moreno AF, Alexis F, Gu FX, Basto PA, Bagalkot V, et al. Co-delivery of hydrophobic and hydrophilic drugs from nanoparticle-aptamer bioconjugates. ChemMedChem. 2007;2:1268–71.

22. Liu SH, Guo YB, Huang RQ, Li JF, Huang SX, Kuang YY, et al. Gene and doxorubicin co-delivery system for targeting therapy of glioma. Biomaterials. 2012;33:4907–16.
23. Mujokoro B, Adabi M, Sadroddiny E, Adabi M, Khosravani M. Nano-structures mediated co-delivery of therapeutic agents for glioblastoma treatment: a review. Mat Sci Eng C-Mater Biol Appl. 2016;69:1092–102.
24. Van der Meel R, Sulheim E, Shi Y, Kiessling F, Mulder WJM, Lammers T. Smart cancer nanomedicine. Nat Nanotechnol. 2019;14:1007–17.
25. Bar-Zeev M, Livney YD, Assaraf YG. Targeted nanomedicine for cancer therapeutics: towards precision medicine overcoming drug resistance. Drug Resist Updat. 2017;31:15–30.
26. Bjornmalm M, Thurecht KJ, Michael M, Scott AM, Caruso F. Bridging bio-nano science and cancer nanomedicine. ACS Nano. 2017;11:9594–613.
27. Mangal S, Gao W, Li TL, Zhou Q. Pulmonary delivery of nanoparticle chemotherapy for thetreatment of lung cancers: challenges and opportunities. Acta Pharmacol Sin. 2017;38:782–97.
28. Huang YZ, Li YP. Cancer nanobiotechnolgy. Acta Pharmacol Sin. 2017;38:735–7.
29. Sun TM, Zhang YS, Pang B, Hyun DC, Yang MX, Xia YN. Engineered nanoparticles for drug delivery in cancer therapy. Angew Chem Int Ed. 2014;53:12320–64.
30. Fenton OS, Olafson KN, Pillai PS, Mitchell MJ, Langer R. Advances in biomaterials for drug delivery. Adv Mater. 2018. https://doi.org/10.1002/adma.201705328.
31. Tong R, Langer R. Nanomedicines targeting the tumor microenvironment. Cancer J. 2015;21:314–21.
32. Lee ES, Gao ZG, Bae YH. Recent progress in tumor pH targeting nanotechnology. J Control Release. 2008;132:164–70.
33. Feng LZ, Dong ZL, Tao DL, Zhang YC, Liu Z. The acidic tumor microenvironment: a target for smart cancer nano-theranostics. Natl Sci Rev. 2018;5:269–86.
34. Piao JG, Gao F, Yang LH. Acid-responsive therapeutic polymer for prolonging nanoparticle circulation lifetime and destroying drug-resistant tumors. ACS Appl Mater Inter. 2016;8:936–44.
35. Piao JG, Gao F, Li YN, Yu L, Liu D, Tan ZB, et al. pH-sensitive zwitterionic coating of gold nanocages improves tumor targeting and photothermal treatment efficacy. Nano Res. 2018;11:3193–204.
36. Yao XM, Chen XF, He CL, Chen L, Chen XS. Dual pH-responsive mesoporous silica nanoparticles for efficient combination of chemotherapy and photodynamic therapy. J Mater Chem B. 2015;3:4707–14.
37. Deng HZ, Zhao XF, Liu JJ, Zhang JH, Deng LD, Liu JF, et al. Synergistic dual-pH responsive copolymer micelles for pH-dependent drug release. Nanoscale. 2016;8:1437–50.
38. Chen Y, Chen HR, Shi JL. In vivo bio-safety evaluations and diagnostic/therapeutic applications of chemically designed mesoporous silica nanoparticles. Adv Mater. 2013;25:3144–76.
39. Rosenholm JM, Mamaeva V, Sahlgren C, Linden M. Nanoparticles in targeted cancer therapy: mesoporous silica nanoparticles entering preclinical development stage. Nanomedicine. 2012;7:111–20.
40. Burns A, Ow H, Wiesner U. Fluorescent core-shell silica nanoparticles: towards "Lab on a Particle" architectures for nanobiotechnology. Chem Soc Rev. 2006;35:1028–42.
41. Benezra M, Penate-Medina O, Zanzonico PB, Schaer D, Ow H, Burns A, et al. Multimodal silica nanoparticles are effective cancer-targeted probes in a model of human melanoma. J Clin Invest. 2011;121:2768–80.
42. Yang PP, Gai SL, Lin J. Functionalized mesoporous silica materials for controlled drug delivery. Chem Soc Rev. 2012;41:3679–98.
43. Tarn D, Ashley CE, Xue M, Carnes EC, Zink JI, Brinker CJ. Mesoporous silica nanoparticle nanocarriers: biofunctionality and biocompatibility. Acc Chem Res. 2013;46:792–801.
44. Slowing II, Trewyn BG, Giri S, Lin VSY. Mesoporous silica nanoparticles for drug delivery and biosensing applications. Adv Funct Mater. 2007. https://doi.org/10.1002/adfm.200601191.
45. Trewyn BG, Giri S, Slowing II, Lin VSY. Mesoporous silica nanoparticle based controlled release, drug delivery, and biosensor systems. Chem Commun. 2007:3236–45. https://doi.org/10.1039/b701744h.
46. Hong CY, Li X, Pan CY. Fabrication of smart nanocontainers with a mesoporous core and a pH-responsive shell for controlled uptake and release. J Mater Chem. 2009;19:5155–60.
47. Wang LY,Huo MF, Chen Y, Shi JL. Tumor microenvironment-enabled nanotherapy. Adv Healthc Mater. 2018. https://doi.org/10.1002/adhm.201701156.
48. Ashley CE, Carnes EC, Epler KE, Padilla DP, Phillips GK, Castillo RE, et al. Delivery of small interfering RNA by peptide-targeted mesoporous silica nanoparticle-supported lipid bilayers. ACS Nano. 2012;6:2174–88.
49. Namiki Y, Fuchigami T, Tada N, Kawamura R, Matsunuma S, Kitamoto Y, et al. Nanomedicine for cancer: lipid-based nanostructures for drug delivery and monitoring. Acc Chem Res. 2011;44:1080–93.
50. Qiu Y, Wu C, Jiang J, Hao YN, Zhao Y, Xu J, et al. Lipid-coated hollow mesoporous silica nanospheres for co-delivery of doxorubicin and paclitaxel: preparation, sustained release, cellular uptake and pharmacokinetics. Mat Sci Eng C-Mater Biol Appl. 2017;71:835–43.
51. Krishnamurthy S, Vaiyapuri R, Zhang LF, Chan JM. Lipid-coated polymeric nanoparticles for cancer drug delivery. Biomater Sci. 2015;3:923–36.
52. He QJ, Gao Y, Zhang LX, Zhang ZW, Gao F, Ji XF, et al. A pH-responsive mesoporous silica nanoparticles-based multidrug delivery system for overcoming multidrug resistance. Biomaterials. 2011;32:7711–20.
53. Luan X, Guan YY, Lovell JF, Zhao M, Lu Q, Liu YR, et al. Tumor priming using metronomic chemotherapy with neovasculature-targeted, nanoparticulate paclitaxel. Biomaterials. 2016;95:60–73.
54. Fei WD, Zhang Y, Han SP, Tao JY, Zheng HY, Wei YH, et al. RGD conjugated liposome-hollow silica hybrid nanovehicles for targeted and controlled delivery of arsenic trioxide against hepatic carcinoma. Int J Pharm. 2017;519:250–62.
55. Kuh HJ, Jang SH, Wientjes MG, Weaver JR, Au JL. Determinants of paclitaxel penetration and accumulation in human solid tumor. J Pharmacol Exp Ther. 1999;290:871–80.
56. Wang J, Lu Z, Gao Y, Wientjes MG, Au JLS. Improving delivery and efficacy of nanomedicines in solid tumors: role of tumor priming. Nanomedicine. 2011;6:1605–20.
57. Zhao ZM, Lou S, Hu Y, Zhu J, Zhang CM. A nano-in-nano polymer-dendrimer nanoparticle-based nanosystem for controlled multidrug delivery. Mol Pharmacol. 2017;14:2697–710.